RSC Advances

PAPER

View Article Online
View Journal | View Issue

Open Access Article. Published on 03 January 2024. Downloaded on 2/17/2026 1:33:08 PM.
This article is licensed under a Creative Commons Attribution-NonCommercial 3.0 Unported Licence.

Cite this: *RSC Adv.*, 2024, **14**, 1431

Ultrafast and simultaneous removal of four tetracyclines from aqueous solutions using waste material-derived graphene oxide-supported cobalt–iron magnetic nanocomposites†

Md Sohag Hossain, [ab] Md Humayun Kabir, *[a] Md Aftab Ali Shaikh,*[ab] Md Anamul Haque [b] and Sabina Yasmin *[a]

Received 7th November 2023
Accepted 12th December 2023

DOI: 10.1039/d3ra07597d

rsc.li/rsc-advances

In this work, a graphene oxide-supported cobalt–iron oxide (GO/Co–Fe) magnetic nanocomposite was successfully synthesized using waste dry cells for the efficient and simultaneous removal of tetracycline (TC), chlortetracycline (CTC), oxytetracycline (OTC), and doxycycline (DTC) from aqueous solutions. The GO/Co–Fe nanocomposite was thoroughly characterized using Fourier transform infrared spectroscopy, vibrating sample magnetometry, X-ray diffraction, field emission scanning electron microscopy, energy-dispersive X-ray spectroscopy, transmission electron microscopy, X-ray photoelectron spectroscopy, and zeta potential analysis. This multi-faceted characterization provided clean insights into the composition and properties of the synthesized nanocomposite. The adsorption of tetracyclines (TCs) was systematically investigated by assessing the influence of critical factors, such as adsorbent dosage, contact duration, initial pH of the solution, initial concentration, and temperature. The GO/Co–Fe adsorbent showed high removal efficiencies of 94.1% TC, 94.32% CTC, 94.22% OTC, and 96.94% DTC within 30 s contact period. The maximum removal efficiency of TCs was found at a low adsorbent dose of 0.15 g L^{-1}. Notably, this superior removal efficiency was achieved at neutral pH and room temperature, demonstrating the adsorbent's efficacy under environmentally viable conditions. The kinetic studies demonstrated that the adsorption process was fitted satisfactorily with the pseudo-second-order model. Additionally, the adsorption behaviour of TCs on the GO/Co–Fe adsorbent was assessed by isotherm models, Langmuir and Freundlich. The experimental data followed the Langmuir isotherm, signifying a monolayer adsorption mechanism on the surface of the adsorbent. The adsorption capacities (q_m) of GO/Co–Fe for TC, CTC, OTC and DTC were determined to be 64.10, 71.43, 72.46 and 99.01 mg g^{-1}, respectively. Importantly, the GO/Co–Fe adsorbent showed reusability capabilities. The super magnetic properties of GO/Co–Fe made it easy to use for several cycles. These results clearly establish GO/Co–Fe as an exceptionally effective adsorbent for the removal of TCs from aqueous systems, highlighting its great potentiality in water treatment applications.

1 Introduction

Antibiotics are extensively used as medical treatments for microbial infections in humans and animals, as well as supplements in animal diets.[1] Antibiotics are almost ubiquitous due to their widespread use. They have been detected in a wide range of ecosystems, including terrestrial and aquatic environments, and even in drinking water sources.[2,3] The advantages of antibiotics in healthcare are unquestionable, yet their excessive use heightens the environmental risks by promoting the evolution of bacterial drug resistance.[4] Therefore, the removal of widely used antibiotics from various aqueous systems has become a crucial concern.

Tetracyclines (TCs), a group of wide-ranging antibiotics, including oxytetracycline (OTC), tetracycline (TC), chlortetracycline (CTC), and doxycycline (DTC), synthesized by actinomycetes, have been employed for many years as additives in animal feed and in both human and veterinary medicine.[5] TCs have a flat structure made up of four interconnected rings with phenol, ketone, and amino groups in each ring.[6] The use of TCs over an extended period of time may promote the emergence of genes that resist antibiotics.[7]

Recently, TC residues have been identified in a diverse array of ecosystems, including sediments, surface waters, soils, marine environments, and even biota samples, due to its

---

[a] *Institute of National Analytical Research and Service (INARS), Bangladesh Council of Scientific and Industrial Research (BCSIR), Dhanmondi, Dhaka-1205, Bangladesh. E-mail: sabinayasmin@bcsir.gov.bd; humayunkabir@bcsir.gov.bd*

[b] *Department of Chemistry, University of Dhaka, Dhaka 1000, Bangladesh. E-mail: aftabshaikh@du.ac.bd*

† Electronic supplementary information (ESI) available. See DOI: **https://doi.org/10.1039/d3ra07597d**

© 2024 The Author(s). Published by the Royal Society of Chemistry

Open Access Article. Published on 03 January 2024. Downloaded on 2/17/2026 1:33:08 PM.
This article is licensed under a Creative Commons Attribution-NonCommercial 3.0 Unported Licence.

overconsumption in human and animal treatment as well as livestock.[6,8] TC pollution in the environment can lead to the emergence of antibiotic resistance genes in microbes, and these microbes can infiltrate the human body *via* the food chain, which might increase drug resistance in the body and endanger people's health and security.[7] Therefore, it is crucial to design a method that effectively removes TC residues from aqueous systems.

Numerous techniques including biological processes, membrane filtration, disinfection electrochemical processes, photolytic degradation, ozonation, coagulation, ion exchange, chlorination, biodegradation, and activated carbon adsorption have been considered to get rid of antibiotics in wastewater.[8–17] However, these approaches are constrained by their high price, poor removal capacity, and complex reaction conditions. Adsorption has gained popularity as a viable antibiotic elimination strategy in recent years. The advantages of the adsorption method are simplicity of use, high efficiency, low cost, excellent repeatability, and the availability of a variety of adsorbents.[18] Thus far, numerous adsorbents including clay and minerals, activated carbon, humic acid, carbon nanotubes, and graphene oxide (GO) have been used.[19–24] Despite the benefits of the adsorption approach for removing antibiotics, it is costly and time-consuming since adsorbent materials are not highly effective and regeneration is difficult.[25]

To address these challenges, it is crucial to develop a cost-efficient, high-performance, and reusable adsorbent with specific functional groups that facilitate selective adsorption *via* various interaction mechanisms. GO-based nanocomposites have excellent properties as adsorbents for removing antibiotics.[26] GO is a distinctive substance that contains a variety of oxygenated functional groups including epoxide, carbonyl, carboxyl, and hydroxyl groups. These functional groups are linked to both the edges and the plane of the GO.[27,28] Because of its significant physical and chemical features, GO has been considered as a hot topic in various fields of research.[29] The oxygen-based functional groups on the GO surface make it a valuable tool for adsorbing, extracting, and separating antibiotics.[30] Adsorbent materials based on GO disperse readily in water because of their tiny particle size and the presence of hydrophilic units on their surface.[31] Once the adsorption process has been concluded, separation of the adsorbent from the aqueous solution is necessary.[32] Conventional separation processes such as filtration and centrifugation suffer from several disadvantages including high costs, intricate operational steps, and extended processing durations. The magnetic separation technique has progressively attracted the attention of various researchers.[31–34] Certain magnetic substances such as Fe_3O_4 and $Co(NO_3)_2$ might be combined with GO, imparting magnetic properties to the adsorbent. This enables the adsorbent to be separated from the mixture through the application of an external magnetic field. Therefore, a composite material based on magnetic nanoparticles and GO effectively enhances the adsorption capabilities of the adsorbent along with the introduction of magnetic properties that facilitate the separation process.

In this study, a magnetically separable GO/Co–Fe nanocomposite was synthesized, which involved the integration of magnetic nanoparticles, Fe_3O_4 and $Co(NO_3)_2$, with GO. The physical and chemical attributes of these nanocomposites were thoroughly investigated by various analytical techniques. The synthesized nanocomposite materials were employed to adsorb TCs from aqueous solutions. The adsorption processes were explored with respect to various factors such as adsorbent dosage, contact duration, pH, TC concentration, and temperature. An adsorption mechanism is proposed based on kinetic and isotherm models. Additionally, the reusability of the as-prepared adsorbent for the removal of TCs was established.

2 Materials and method

2.1 Chemicals

Tetracycline (CAS: 64-75-5), chlortetracycline (CAS: 64-72-2), oxytetracycline (CAS: 2058-46-0), and doxycycline (CAS: 24390-14-5) with a purity of ≥ 95.0% were obtained from Sigma-Aldrich, Switzerland. LC-MS-grade acetonitrile (ACN) and formic acid (FA) were procured from AppliChem GmbH, Germany. Potassium permanganate ($KMnO_4$; CAS: 7722-64-7) with a purity of ≥ 99.0% and sulfuric acid (H_2SO_4; CAS: 7664-93-9), with a grade of 95–97% were obtained from Scharlau, Spain. The chemicals 85% phosphoric acid (H_3PO_4; CAS: 7664-38-2), ethanol (CAS: 64-17-5) with a purity of ≥ 99.5%, 37% hydrochloric acid (HCl; CAS: 7647-01-0) and 30% hydrogen peroxide (H_2O_2; CAS: 7722-84-1) were purchased from JANSSEN-CHEMICA, Sigma-Aldrich, AppliChem, and Sigma-Aldrich, respectively. All the solutions were prepared using Milli-Q deionized (DI) water.

2.2 Instruments

The TCs, before and after adsorption, were analysed using an Agilent LC module (1290 Infinity II) coupled with a triple quadrupole mass spectrometer (6420LC/TQ). For the separation of analytes, a ZORBAX RRHD Eclipse Plus C18 column (2.1 × 100 mm, 1.8 μm particle size) was employed. The mobile phase was composed of a mixture of 0.1% FA in DI water (A) and ACN (B). An isocratic mobile phase composed of 50% A and 50% B with a total flow rate of 0.3 mL min^{-1} was utilized. Multiple reaction monitoring was employed in the positive electron spray ionization mode (ESI+) with specific mass transitions for ion qualification and quantification. In addition, XRD patterns were acquired using an X-ray diffractometer (model: SmartLab SE, Rigaku, Japan) equipped with a Cu Kα source (1.54 Å). The FTIR spectra of GO and GO/Co–Fe recorded using a SHIMADZU IRAffinity-1 spectrometer. The surface morphology and elemental composition of GO/Co–Fe were observed using a transmission electron microscope (TEM) equipped with an energy-dispersive spectrometer (EDX) (TEM-EDX; Talos F200X, Thermo Fisher Scientific, with an accelerating voltage of 200 kV) and a field emission scanning electron microscope (FE-SEM, JEOL-JSM-7610F, operating at 0.1–30 kV, located in the Netherlands). The chemical composition and valence states of GO/Co–Fe were analyzed by X-ray photoelectron spectroscopy (XPS;

© 2024 The Author(s). Published by the Royal Society of Chemistry

Open Access Article. Published on 03 January 2024. Downloaded on 2/17/2026 1:33:08 PM.
This article is licensed under a Creative Commons Attribution-NonCommercial 3.0 Unported Licence.

K-Alpha, Thermo Scientific, UK). To determine the magnetic properties of the adsorbent, vibrating sample magnetometry (VSM) was used (Lakeshore, USDA), and the hysteresis loop of the dried samples was generated. Surface charge measurements of the GO/Co–Fe nanocomposite were performed using a zeta potential analyzer (model: HORIBA Scientific, SZ-100V2, located in Japan) over a pH range spanning from 2 to 11.

2.3 Collection of graphite powder

Graphite powder was extracted from waste dry cells, which were collected from residential areas and markets. The procedure of the graphite powder collection process has been described in our previous study.[28] In brief, graphite rods were collected by the gentle deconstruction of the dry cells. The graphite rods were cleaned by rubbing paper and repeated washes with DI water to eliminate impurities. The cleaned graphite rods were air-dried and finely powdered using a mortar and pestle. To eliminate the additional impurities, the graphite powder was treated with Aqua Regia and washed several times with DI water until it attained a neutral pH. Finally, the purified graphite powder was dried at 60 °C for 24 h.

2.4 Synthesis of GO

GO was prepared from the reclaimed graphite powder by the improved Hummer's method.[35,36] To outline the procedure briefly, 240 mL of H_2SO_4 and 28 mL of H_3PO_4 (9 : 1 v/v ratio) were mixed in a 500 mL round-bottom flask. In a gradual manner, 2 g of graphite powder was introduced into the mixture with continuous stirring. Subsequently, 6 g of $KMnO_4$ was slowly added to this mixture. The mixture was heated and continuously stirred at 50 °C for 2 h until turned into dark green. After cooling the reaction mixture to room temperature and further reducing the temperature in an ice bath, 400 mL of DI water and 18 mL of 30% H_2O_2 were slowly added with stirring to remove excess $KMnO_4$. The reaction was then halted and the mixture was centrifuged at 4000 rpm. The resulting precipitate was washed with DI water and subjected to further purification by washing with 30% HCl to eliminate metallic impurities. Subsequently, it was washed with DI water again to eliminate chlorides and finally washed with ethanol to remove organic residues. The resulting GO was dried at 45 °C for 24 h in a vacuum drying oven.

2.5 Synthesis of GO/Co–Fe

A GO/Co–Fe composite was synthesized in a 250 mL round-bottom flask by dissolving $Co(NO_3)_2 \cdot 6H_2O$, $FeSO_4 \cdot 7H_2O$, and $Fe_2(SO_4)_3 \cdot nH_2O$ in DI water in a mole ratio of 1/1/2. The mixture was agitated using a magnetic stirrer at 40 °C for 25 min. Subsequently, an aqueous suspension of 100 mg GO was added to the mixture, and the pH was adjusted to ∼10. The mixture was then heated at 85 °C for 1 h. After cooling, the resulting precipitate was thoroughly washed with both ethanol and DI water until it reached a neutral pH. The GO/Co–Fe composite was dried in a vacuum drying oven at 60 °C for 24 h (Scheme 1).

2.6 Adsorption studies

Aqueous solutions of tetracyclines (TC, CTC, OTC, and DTC) were prepared with known concentrations. A precise and predetermined quantity of the GO/Co–Fe adsorbent was added into the solution, followed by shaking the samples for a designated period at 250 rpm under constant temperature conditions. After the predefined contact period, the samples were centrifuged at 4000 rpm for 10 minutes to separate the adsorbent from the solution. The solution was subsequently passed through a 0.22 μm CHROMAFIL® Xtra syringe filter to eliminate the remaining particulate matters. The concentration of the TC before and after adsorption was determined by LC-MS/MS. The batch experiments were conducted using various amounts of the adsorbent (0.5, 1.0, 2.0, 3.0, 5.0, 7.0, 10, and 12 mg) at pH of 2.0, 3.0, 6.0, 7.0, 8.0, 9.0, and 10.0 with initial concentrations of TCs (0.2, 0.4, 0.6, 1.0, 1.2, 1.5, and 2.0 ppm). The pH was adjusted by adding either 0.1 M HCl or 0.1 M NaOH to the solution. In kinetics investigations, the contact time was varied from 0.5 to 90 min, while in isotherm studies, the initial concentration was regulated from 2 to 10 ppm at three different temperatures (30, 40, and 50 °C). For the regeneration study, the adsorbent was separated by utilizing an external magnetic field after the adsorption of TCs. The resulting adsorbent was treated with methanol and washed with distilled water, followed by drying at 50 °C. The removal percentage, adsorbed amount at time t (q_t) and at equilibrium time (q_e), were calculated using the eqn (1)–(3), respectively:

$$\text{Removal percentage} = \frac{C_0 - C_t}{C_0} \times 100\% \quad (1)$$

$$q_t = \frac{C_0 - C_t}{M} \times V \quad (2)$$

$$q_e = \frac{C_0 - C_e}{M} \times V \quad (3)$$

where C_0, C_t, and C_e stand for the initial, at time t, and equilibrium concentrations of TC solutions, measured in mg L^{-1}. M

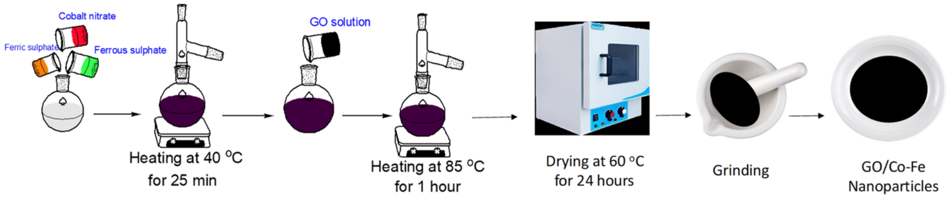

Scheme 1 Schematic of the GO/Co–Fe synthesis.

Open Access Article. Published on 03 January 2024. Downloaded on 2/17/2026 1:33:08 PM.
This article is licensed under a Creative Commons Attribution-NonCommercial 3.0 Unported Licence.

represents the amount of adsorbent, measured in g. V signifies the volume of TC solutions, measured in L.

3 Results and discussion

3.1 Characterization of GO/Co–Fe

3.1.1 X-ray diffraction (XRD). The X-ray diffraction (XRD) patterns for synthesised GO and GO/Co–Fe are shown in Fig. 1(a). The diffractogram of GO exhibits several reflections at $2\theta = 11.72°$, $26.71°$, and $42.54°$ mentioned with their corresponding planes (002), (110), and (110), respectively. At $2\theta = 11.72°$, a distinct and sharp reflection is observed in GO, attributed to the diffraction of the (002) plane.[37] This diffraction pattern corresponds to an interplanar spacing of 0.75 nm, as calculated using Bragg's equation. This specific pattern is indicative of the presence of oxygen-containing functional groups that result from the oxidation process. The diffraction pattern of GO/Co–Fe shows five reflections at $2\theta = 30.32$, $35.41°$, $43.16°$, $57.33°$ and $62.57°$ marked with their corresponding planes (220), (311), (400), (511), and (440) having interlayer spacings of respectively 0.28, 0.25, 0.21, 0.16, and 0.15 nm. At $2\theta = 35.4°$, the sharp peak of GO/Co–Fe is observed due to the diffraction of the (311) plane, revealing an interplanar spacing of 0.25 nm.[38] The interlayer spacing of 0.25 nm observed in the GO/Co–Fe composite differs from the typical interlayer spacing of GO, which is around 0.745 nm. The reduced interplanar spacing in the GO/Co–Fe composite may be due to the structural modification of the GO layers. The presence of Co–Fe nanoparticles could result in the compression or shrinkage of the interlayer spacing. These modifications may arise from interactions between the GO layers and the incorporated nanoparticles, leading to changes in the interlayer arrangement and bonding. GO/Co–Fe particles have small sizes, as evidenced by the reduced height of the peaks. These results firmly suggested that GO/Co–Fe should have a different chemical composition than that of pure GO.

3.1.2 Fourier transform infrared (FTIR) spectroscopy. The Fourier transform infrared (FTIR) spectra of both GO and GO/Co–Fe are depicted in Fig. 1(b). In the FTIR spectrum of GO, characteristic peaks are observed at 3414 cm^{-1} (O–H stretching), 1227 cm^{-1} (O–H bending), and 1720 cm^{-1} (C=O stretching of carboxyl group). Strong peaks are also present at 1585 cm^{-1} (aromatic C=C stretching) and 1052 cm^{-1} (C–O–C stretching of epoxy groups).[39] However, in the FTIR spectrum of GO/Co–Fe, some notable differences are observed. The absorption peak for C=O stretching in the carboxyl group weakens compared to that of GO. The peaks for aromatic C=C stretching and epoxy groups also shift to 1620 cm^{-1} and 1110 cm^{-1}, respectively. These peak position shifts suggest strong interactions between the Co–Fe nanoparticles and the functional groups of GO. Furthermore, the presence of additional peaks in the FTIR spectrum of GO/Co–Fe indicates the incorporation of Co–Fe

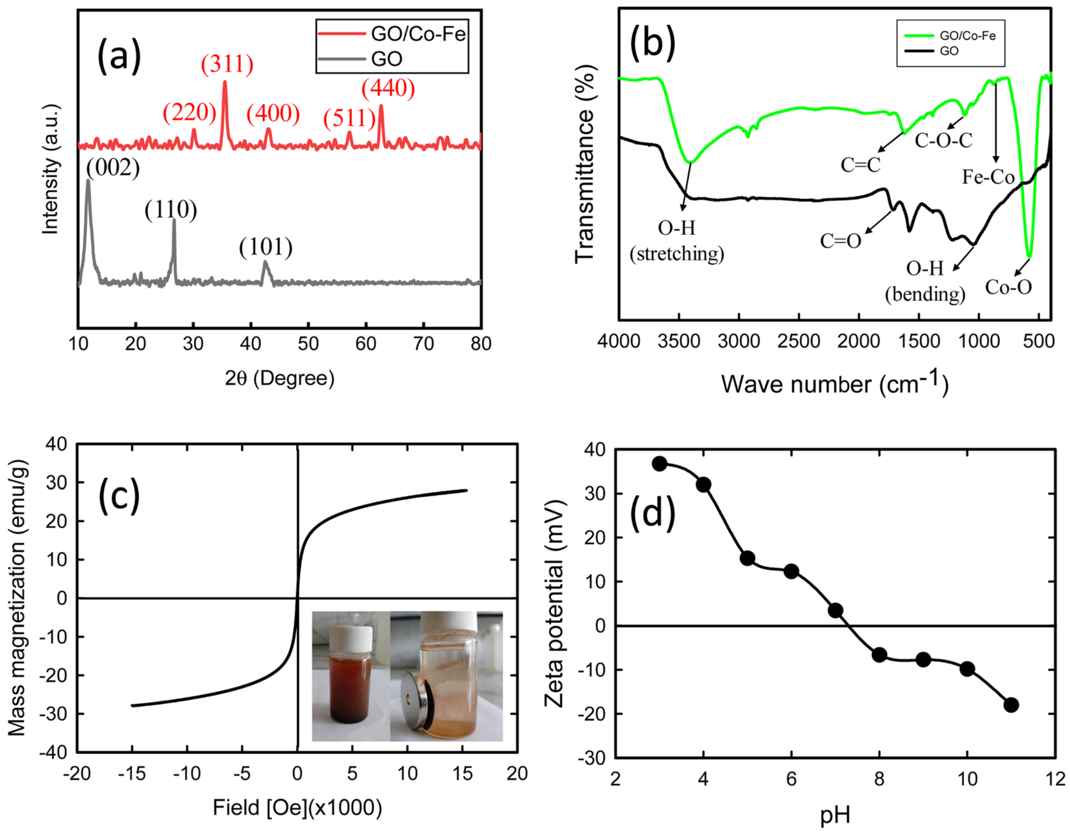

Fig. 1 (a) XRD pattern of GO and GO/Co–Fe. (b) FTIR spectra of GO and GO/Co–Fe. (c) Magnetization curve (the right inset illustrates the magnetic separation of GO/Co–Fe). (d) Zeta potential of GO/Co–Fe as a function of pH.

© 2024 The Author(s). Published by the Royal Society of Chemistry

Open Access Article. Published on 03 January 2024. Downloaded on 2/17/2026 1:33:08 PM.
This article is licensed under a Creative Commons Attribution-NonCommercial 3.0 Unported Licence.

nanoparticles. Specifically, the stretching vibration of Fe–Co appears at 875 cm^{-1}, while the peak for Co–O stretching is observed at 570 cm^{-1}.[40] These peaks indicate the presence of Fe–Co and Co–O bonds, suggesting the successful incorporation of Co–Fe nanoparticles into the GO surface.

3.1.3 Vibrating sample magnetometry (VSM). The investigation of the magnetic properties of the synthesized GO/Co–Fe composite was performed using a vibrating sample magnetometer (VSM), and the results are presented in Fig. 1(c). The M–H hysteresis loop obtained from the plot shows important magnetic characteristics of the composite. The magnetic saturation value of GO/Co–Fe, determined from the hysteresis loop, was found to be 27.82 emu g^{-1}. This value represents the maximum magnetization that the composite can attain under the applied magnetic field. The absence of coercivity and remanence in the magnetization curve indicates that GO/Co–Fe does not exhibit permanent magnetism. This observation suggests that the composite displays superparamagnetic behaviour. To further confirm the superparamagnetic nature of GO/Co–Fe, an image was inserted right in Fig. 1(c), demonstrating the adsorption of the GO/Co–Fe adsorbent onto the magnetized wall of the reaction vessel when exposed to an external magnetic field. This observation verifies the magnetic responsiveness and ability of the GO/Co–Fe composite to be quickly separated using a magnetic field.

3.1.4 Zeta potential measurements. The results of zeta potential measurements concerning pH variation are presented in Fig. 1(d). The observation indicates that the zeta potential is positive up to pH 7.2. This suggests that the surface of GO/Co–Fe has a net positive charge in the pH range below 7.2. The positively charged zeta potential can be ascribed to the existence of surface species with positive charges at lower pH values. The point of zero charge (PZC) of the GO/Co–Fe composite is indicated by the zeta potential becoming zero at pH 7.2. At this particular pH, there is an approximate balance between the number of positively and negatively charged functional groups or surface species on the composite. However, when the pH of solution surpasses 7.2, the zeta potential turns negative. This change towards a negative zeta potential is due to the deprotonation of functional groups or surface species on the composite, causing an escalation in negative charges on the surface of the GO/Co–Fe composite.

3.1.5 Field emission scanning electron microscopy (FESEM). The representative FESEM images of GO and GO/Co–Fe are shown in Fig. 2(a) and (b). The image in Fig. 2(a) demonstrates the layered structure of GO with a wrinkled appearance, which may be due to the existence of oxygenated functional groups. These wrinkles can be ascribed to the introduction of defects and functional groups during the oxidation process, leading to non-planar and undulating surface morphology. The FESEM image of GO/Co–Fe shows a rough surface with clusters of various sizes distributed on the GO sheets (Fig. 2(b)). The EDX spectral analysis presented in Fig. 2(c) and (d) provides important information about the elemental composition of GO and GO/Co–Fe, respectively. The results of the EDX analysis confirm that GO/Co–Fe contains carbon (C) and oxygen (O) as essential components of GO and the presence of Fe and Co with their respective atomic fractions, suggesting that the nanoparticles have been effectively incorporated into the GO surface. The rough surface morphology can arise from the interaction and aggregation of the nanoparticles on the GO sheets, contributing to a more heterogeneous and textured composite structure. The EDX analysis also supports the observations obtained from FTIR analysis that GO/Co–Fe possesses oxygenated functional groups, as evidenced by the atomic and mass fractions of oxygen. It is worth noting that the

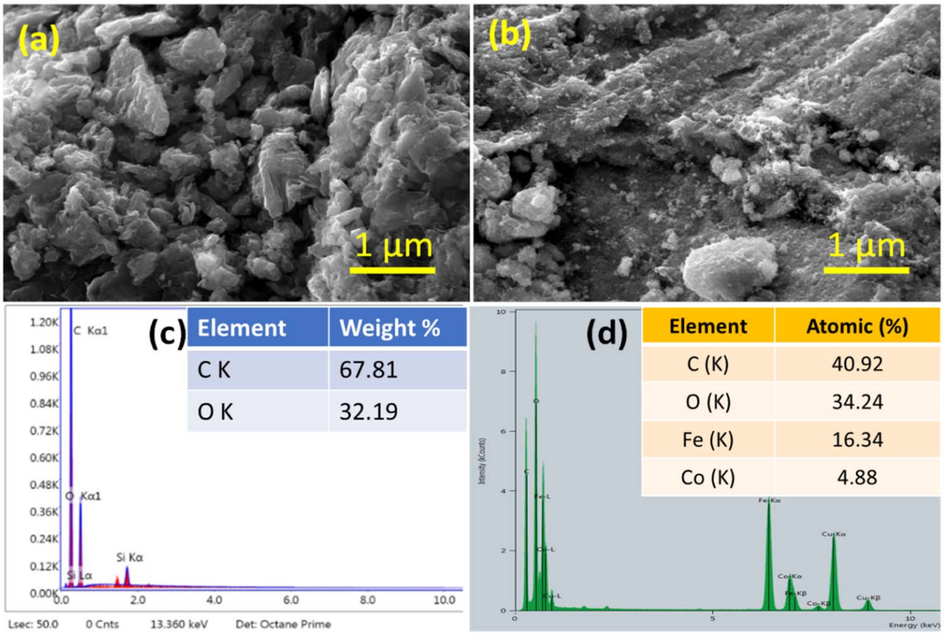

Element	Weight %
C K	67.81
O K	32.19

Element	Atomic (%)
C (K)	40.92
O (K)	34.24
Fe (K)	16.34
Co (K)	4.88

Fig. 2 (a) FESEM image of GO and (b) GO/Co–Fe. (c) EDX spectra of GO and (d) GO/Co–Fe.

Open Access Article. Published on 03 January 2024. Downloaded on 2/17/2026 1:33:08 PM.
This article is licensed under a Creative Commons Attribution-NonCommercial 3.0 Unported Licence.

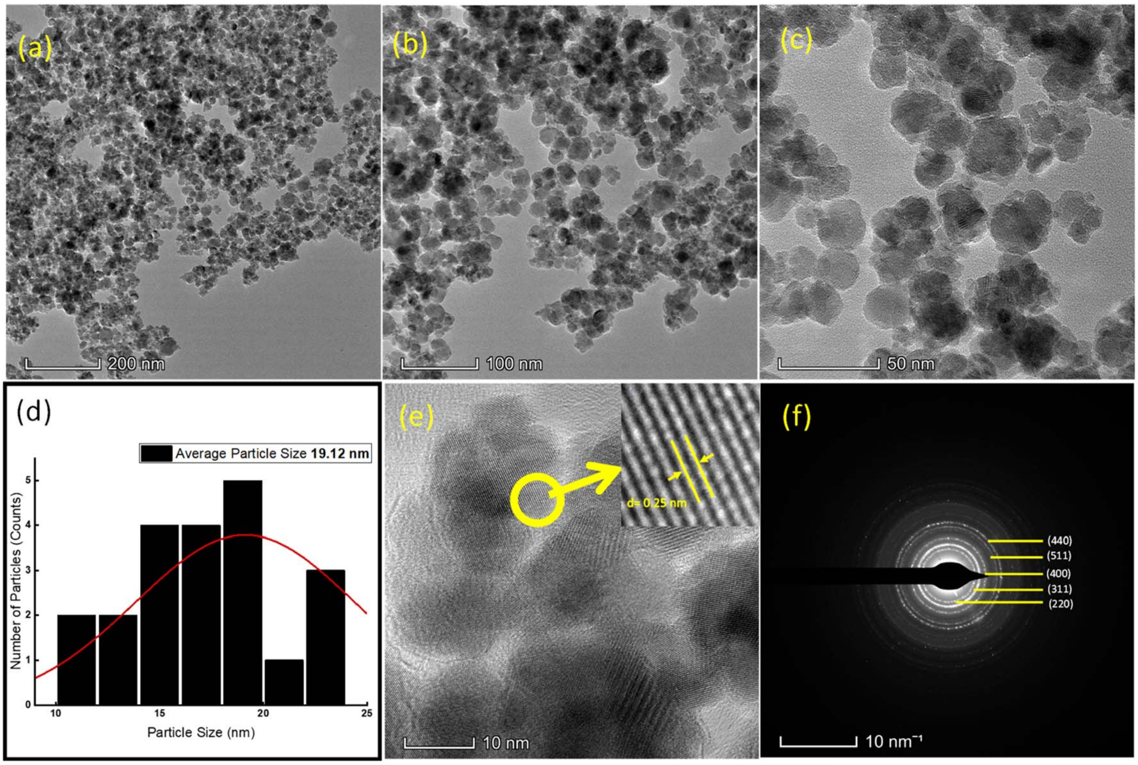

Fig. 3 TEM images of GO/Co–Fe at (a) 200 nm, (b) 100 nm, (c) and 50 nm. (d) Particle size distribution (e) at 10 nm marked with an interplanar spacing of 0.25 nm. (f) SAED pattern.

presence of Cu in the spectrum is a result of the EDX analysis being performed on a Cu grid. This indicates that the EDX analysis captured the background signal from the Cu grid itself.

3.1.6 Transmission electron microscopy (TEM). The results obtained from TEM analysis are shown in Fig. 3(a)–(f). The TEM images in Fig. 3(a)–(c) illustrate the structure of the GO/Co–Fe composite at different magnifications. The spherical nanoparticles represent the clear deposition of Co–Fe NPs on the surface of GO. The particle size distribution analysis reveals that the nanoparticles in GO/Co–Fe have an average particle size of 19.2 nm (Fig. 3(d)). The interlayer spacing of GO/Co–Fe was calculated to be 0.25 nm (Fig. 3(e)) similar to the interplanar spacing obtained from XRD analysis, corresponding to the diffraction of the (311) plane. These results indicate the arrangement and packing of the nanoparticles on the surface of GO. In Fig. 3(f), the selected area electron diffraction (SAED) pattern for GO/Co–Fe displays diffraction rings corresponding to the (220), (311), (400), (511), and (400) Miller indices, which are consistent with the result obtained from XRD. This provides strong evidence of the crystalline nature of the composite, indicating the presence of ordered arrangements of Co–Fe nanoparticles within the GO matrix.

3.1.7 X-ray photoelectron spectroscopy (XPS). The broad XPS spectrum (Fig. 4(a)) and detailed spectra for C 1s, O 1s, Co 2p, and Fe 2p (Fig. 4(b)–(e)) provide information regarding the chemical composition and oxidation states of the elements in the GO/Co–Fe composite. As shown in Fig. 4(a), the wide spectrum of GO/Co–Fe displayed peaks of C 1s, O 1s, Fe $2p_1$, Fe $2p_3$, Co $2p_1$, and Co $2p_3$ at binding energies of 285.14, 530.85, 724.08, 711.08, 796.44, and 781.08 eV, respectively. The C 1s spectrum displays peaks at binding energies of 284.79 eV (C–C), 286.49 eV (C–O), and 288.59 eV (O–C=O) (Fig. 4(b)).[41] These peaks indicate the presence of carbon–carbon (C–C) bonds, carbon–oxygen (C–O) bonds, and oxygen–carbon double bonds (O–C=O), respectively.[42–44] The observed peaks confirm the presence of oxygenated functional groups on the GO/Co–Fe composite. Fig. 4(c) presents the O 1s spectrum, which exhibits peaks at 503.11 eV (metal oxides), 531.64 eV (C–O), and 533.19 eV (C=O)[45,46] The results further support the presence of oxygenated functional groups and metal oxide species in the GO/Co–Fe composite. The Co 2p spectra in Fig. 4(d) shows two peaks at 780.43 (Co $2p_{3/2}$), and 796.48 eV (Co $2p_{1/2}$), indicating the presence of cobalt atom as +2 oxidation state.[47] The appearance of these peaks also confirm that cobalt has been effectively deposited on the surface of GO.[48] Similarly, the Fe 2p spectra (Fig. 4(e)) show two peaks at 710.78 (Fe $2p_{3/2}$), and 724.48 eV (Fe $2p_{1/2}$), suggesting the presence of iron atoms in the +3 oxidation state.[49] Therefore, it is revealed that a successful deposition of cobalt and iron on GO has occurred.

3.2 Adsorption of tetracyclines by the synthesized GO/Co–Fe nanocomposite

To optimize the adsorption conditions for the removal of TCs (TC, CTC, OTC, and DTC) using the synthesized GO/Co–Fe

© 2024 The Author(s). Published by the Royal Society of Chemistry

Open Access Article. Published on 03 January 2024. Downloaded on 2/17/2026 1:33:08 PM.
This article is licensed under a Creative Commons Attribution-NonCommercial 3.0 Unported Licence.

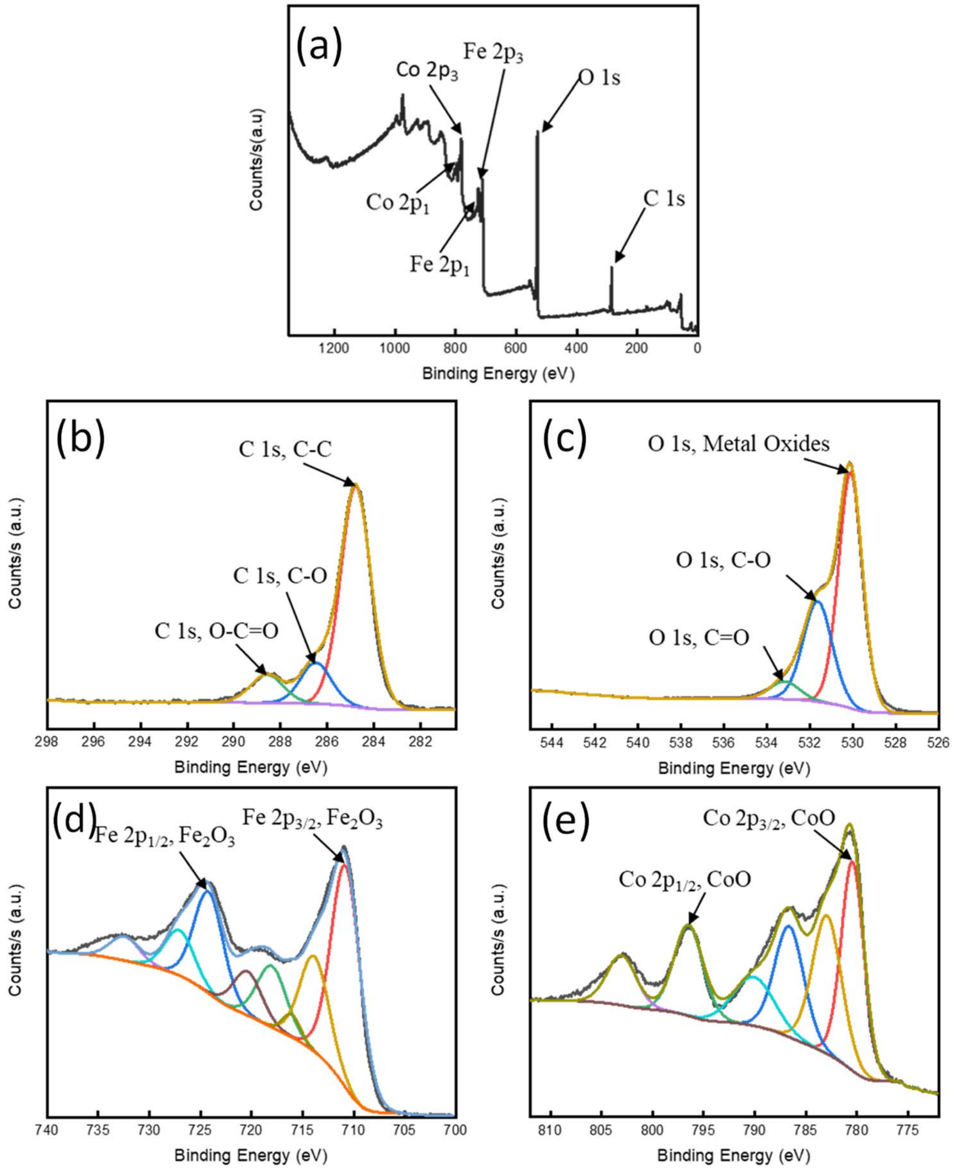

Fig. 4 (a) XPS spectrum of survey; high-resolution spectra of (b) C 1s, (c) O 1s, (d) Co 2p, and (e) Fe 2p.

Table 1 Parameters derived from kinetic models

Kinetic model (liner)	Antibiotic	Parameters		
Pseudo-first order	TC	k_1 (g mg^{-1} min^{-1}) = 0.0038	q_e (mg g^{-1}) = 0.0990	$R^2 = 0.1174$
	CTC	k_1 (g mg^{-1} min^{-1}) = 0.0029	q_e (mg g^{-1}) = 0.0959	$R^2 = 0.2021$
	OTC	k_1 (g mg^{-1} min^{-1}) = 0.0040	q_e (mg g^{-1}) = 0.1093	$R^2 = 0.1294$
	DTC	k_1 (g mg^{-1} min^{-1}) = 0.0002	q_e (mg g^{-1}) = 0.0954	$R^2 = 0.0003$
Pseudo-second order	TC	k_2 (g mg^{-1} min^{-1}) = 0.9684	q_e (mg g^{-1}) = 1.2681	$R^2 = 0.9991$
	CTC	k_2 (g mg^{-1} min^{-1}) = 1.9040	q_e (mg g^{-1}) = 1.2611	$R^2 = 0.9998$
	OTC	k_2 (g mg^{-1} min^{-1}) = 0.9960	q_e (mg g^{-1}) = 1.2604	$R^2 = 0.9991$
	DTC	k_2 (g mg^{-1} min^{-1}) = 1.1393	q_e (mg g^{-1}) = 1.2506	$R^2 = 0.9994$
Elovich	TC	α (g mg^{-1} min^{-1}) = -5.28×10^{-35}	β (mg g^{-1}) = −59.523	$R^2 = 0.8347$
	CTC	α (g mg^{-1} min^{-1}) = -4.00×10^{-69}	β (mg g^{-1}) = −122.25	$R^2 = 0.4843$
	OTC	α (g mg^{-1} min^{-1}) = -2.50×10^{-38}	β (mg g^{-1}) = −66.225	$R^2 = 0.3945$
	DTC	α (g mg^{-1} min^{-1}) = -1.22×10^{-24}	β (mg g^{-1}) = −40.650	$R^2 = 0.6046$
Intraparticle diffusion	TC	k_i (mg g^{-1} min$^{-0.5}$) = −0.0141	C_i (mg g^{-1}) = 1.2681	$R^2 = 0.8267$
	CTC	k_i (mg g^{-1} min$^{-0.5}$) = −0.0063	C_i (mg g^{-1}) = 1.2527	$R^2 = 0.3993$
	OTC	k_i (mg g^{-1} min$^{-0.5}$) = −0.0115	C_i (mg g^{-1}) = 1.2508	$R^2 = 0.3190$
	DTC	k_i (mg g^{-1} min$^{-0.5}$) = −0.0194	C_i (mg g^{-1}) = 1.2760	$R^2 = 0.5260$

© 2024 The Author(s). Published by the Royal Society of Chemistry

Open Access Article. Published on 03 January 2024. Downloaded on 2/17/2026 1:33:08 PM.
This article is licensed under a Creative Commons Attribution-NonCommercial 3.0 Unported Licence.

composite as the adsorbent, the investigation was carried by regulating the adsorbent dosage, contact time, pH, and concentration. A table with all treatments (combinations of levels of the factors) is presented in ESI† (Table 1).

3.2.1 Effect of the adsorbent dose. The removal efficiency of TCs using GO/Co–Fe was determined by varying the amount of adsorbent, ranging from 0.5 to 12 mg. With the increase in adsorbent dose from 0.5 to 3 mg, a dramatic improvement in the removal efficiency of TCs (10 to 92%) was observed (Fig. 5(a)). This is due to the increase in the amount of GO/Co–Fe adsorbent that provides a greater number of binding sites available for the adsorption of TCs. Nevertheless, once the adsorbent dose exceeded 3 mg, the removal efficiency reached a plateau and remained steady, which specifies the adsorption equilibrium. Conversely, the adsorbed amount (q_e) exhibited a rapid decline at lower adsorbent doses, followed by a gradual increase at higher adsorbent doses. With the rise in adsorbent dosage, there was an increased number of interactions between the adsorbent and adsorbate, leading to aggregation. However, this process eventually slowed down as active sites became occupied by the adsorbate. Considering the significant adsorbed amount and the efficient utilization of the adsorbent, a dose of 0.15 g L^{-1} was established as the optimal adsorbent dose.

3.2.2 Effect of contact time. To explore the effect of contact time on TC removal, experiments were conducted over a range of 0.5 to 20 min of contact time. Fig. 5(b) shows that within 30 s, 94.1% TC, 94.32% CTC, 94.22% OTC, and 96.94% DTC removal were completed, and with time, it slightly decreased. The rapid and efficient adsorption may be due to the abundance of available active sites on GO/Co–Fe that were initially unoccupied, facilitating easy adsorption at these sites. Adsorption was almost constant for up to 20 min. This indicates that the adsorbent surface reached its saturation point, and further adsorption of adsorbate was not possible. Therefore, a contact time of 30 s was determined as the optimal duration for the adsorption process. The high removal efficiency can be attributed to the versatile nature of GO/Co–Fe as an adsorbent. This possesses the capability to adsorb through various mechanisms, including the formation of hydrogen bonds, electrostatic interactions, and electron donor–acceptor interactions[50] (ESI, Fig. S1†).

3.2.3 Effect of pH. The pH plays an important role in affecting the ionisation efficiency of TCs, the surface charge of the adsorbent, and the efficiency of binding sites on the adsorbent. The removal percentages of TCs were assessed through the batch experiments at pH 2–10, as shown in Fig. 5(c).

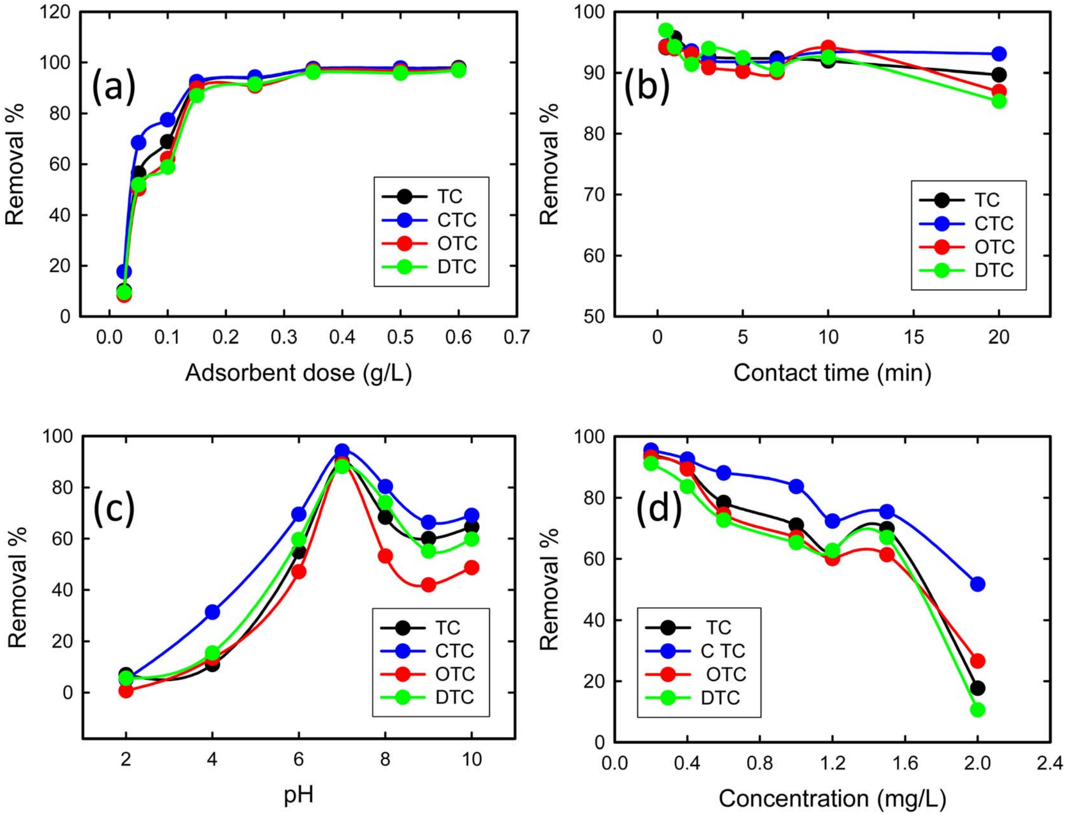

Fig. 5 (a) Effect of the adsorbent dose on the adsorption of tetracyclines from aqueous solutions onto the GO/Co–Fe composite ($C_0 = 200$ ppb, $t = 30$ min, shaking = 250 rpm, $T = 25$ °C). (b) Effect of time on the adsorption of tetracyclines from the aqueous solution by GO/Fe–Co ($C_0 =$ 200 ppb, GO/Co–Fe = 0.15 g L^{-1}, shaking = 250 rpm, $T = 25$ °C, pH = 7). (c) Effect of pH on the adsorption of tetracyclines from the aqueous solution by GO/Co–Fe ($C_0 = 200$ ppb, GO/Co–Fe = 0.15 g L^{-1}, $t = 0.5$ min, shaking = 250 rpm, $T = 25$ °C). (d) Effect of concentration on the adsorption of tetracyclines from the aqueous solution by GO/Co–Fe ($C_0 = 200$ ppb, GO/Co–Fe = 0.15 g L^{-1}, $t = 0.5$ min, pH = 7, shaking = 250 rpm, $T = 25$ °C).

© 2024 The Author(s). Published by the Royal Society of Chemistry

Open Access Article. Published on 03 January 2024. Downloaded on 2/17/2026 1:33:08 PM.
This article is licensed under a Creative Commons Attribution-NonCommercial 3.0 Unported Licence.

The removal efficiency steadily increased from 7 to 90% for TC, 5 to 94% for CTC, 0.7 to 89% for OTC, and 5 to 88% for DTC with the increase in pH from 2 to 7. Upon further increments in pH, a decrease in removal percentage was observed. At pH 7, the adsorption capacity was maximum. This was mostly connected to the chemical structure of TCs, additionally to the electric charge on the surface of the adsorbent. In GO/Co–Fe, the surface remains in neutralised form when dispersed in water due to the presence of oxygenated groups along with cobalt and iron cations. The TCs can exist in three different states depending on the pH: cationic at pH < 3.3, zwitterionic at pH 3.3–7.68, and anionic at pH > 7.68.[38] At pH 7, the interaction between the neutral adsorbent (GO/Co–Fe) and the zwitterionic adsorbate (TCs) involves a combination of electrostatic attractions, hydrogen bonding, and van der Waals forces. Zwitterions can interact efficiently with neutral adsorbents through their charged functional groups, leading to maximum adsorption. Considering the maximum removal efficiency, the optimal pH was chosen as 7.

3.2.4 Effect of concentration. The impact of concentration on the removal efficiency of TCs with the GO/Co–Fe adsorbent was investigated by varying the antibiotic concentration within the range of 0.2–2.0 mg L^{-1} (Fig. 5(d)). For the TC concentration of 0.2 mg L^{-1}, the removal efficiencies of TC, CTC, OTC, and DTC were 93.91%, 95.51%, 93.21%, and 91.12%, respectively. This suggests that the adsorbent exhibited excellent performance in the removal of TCs, even at low initial concentrations. However, as the antibiotic concentration exceeded 0.2 mg L^{-1}, the removal efficiency declined. This indicates that higher initial concentrations of TCs led to reduced removal efficiency. The reduction in removal efficiency with the increase in concentration can be attributed to the limited available adsorption sites, saturation of the adsorbent's binding capacity, and competition between TC molecules for adsorption sites. Considering the higher removal efficiency, 0.2 mg L^{-1} was fixed as the optimal concentration of the antibiotic.

3.2.5 Kinetic studies. To understand the adsorption mechanism, the experimental data were subjected to analysis using several kinetic models such as the Lagergren pseudo-first-order (Fig. 6(a)), Ho pseudo-second-order (Fig. 6(b)), Elovich (Fig. 6(c)), and the Weber–Morris intraparticle diffusion model (Fig. 6(d)). The linearized equations for these models are presented in eqn (4)–(7):

$$\ln(q_e - q_t) = \ln q_e - k_1 t \tag{4}$$

$$\frac{1}{q_t} = \frac{1}{2k_2 {q_e}^2} + \frac{1}{q_e} t \tag{5}$$

$$q_t = \frac{\ln \alpha\beta}{\beta} + \frac{1}{\beta} \ln t \tag{6}$$

$$q_t = k_i t^{0.5} + C_i \tag{7}$$

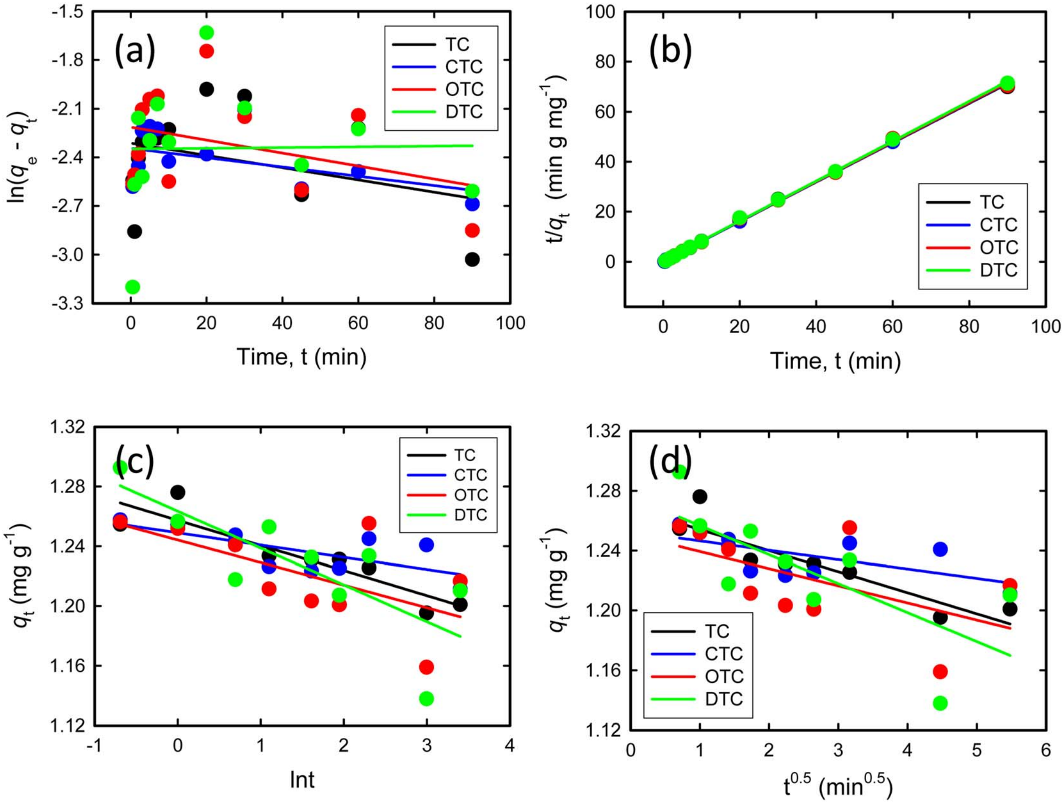

Fig. 6 (a) Pseudo-first-order kinetic model. (b) Pseudo-second-order kinetic model. (c) Elovich kinetic model. (d) Weber–Morris intraparticle diffusion model (C_0 = 200 ppb, pH = 7, GO/Co–Fe = 0.15 g L^{-1}, t = (0.5–90) mins, shaking = 250 rpm, T = 25 °C).

© 2024 The Author(s). Published by the Royal Society of Chemistry

Open Access Article. Published on 03 January 2024. Downloaded on 2/17/2026 1:33:08 PM.
This article is licensed under a Creative Commons Attribution-NonCommercial 3.0 Unported Licence.

where q_e represents the amount adsorbed at equilibrium in mg g^{-1}, q_t denotes the amount adsorbed at time t in mg g^{-1}, k_1 is the rate constant associated with the pseudo-first-order model, expressed in g mg^{-1} min^{-1}, k_2 corresponds to the rate constant linked to the pseudo-second-order model, also measured in g mg^{-1} min^{-1}, α is related to the initial adsorption rate, given in mg g^{-1} min^{-1}, β is associated with the surface coverage and activation energy for chemisorption, in g mg^{-1}, k_i represents the rate constant connected to the intraparticle diffusion model, expressed in mg g^{-1} $min^{-0.5}$, and C_i is a constant that is proportional to the boundary layer thickness, in mg g^{-1}.

The parameters obtained from kinetic models are shown in Table 1. The pseudo-second-order kinetic model, illustrated in Fig. 6(b), exhibits a notably higher correlation coefficient (R^2) of 0.999. These high correlation coefficients indicate a strong agreement between the experimental data and the linear curve fitting equation of the pseudo-second-order kinetic model. The model effectively characterises the adsorption pattern and the speed at which TCs are taken up by the GO/Co–Fe adsorbent, suggesting that the adsorption process is most accurately described by the second-order kinetics and that the adsorption process is likely governed by chemisorption, where the rate-limiting step involves chemical interactions between the adsorbate molecules and the adsorbent surface.

3.2.6 Isotherm studies. Adsorption isotherm models provide valuable insights into the adsorption mechanism, the characteristics of active sites, and the adsorption capacity of an adsorbent. To examine the adsorption isotherms, the experimental data were analyzed using the Langmuir and Freundlich isotherm models. The linear expressions for the Langmuir and Freundlich models are represented by eqn (8) and (9):

$$\frac{C_e}{q_e} = \frac{1}{K_L q_m} + \frac{C_e}{q_m} \tag{8}$$

$$\ln q_e = \ln K_F + 1/n \ln C_e \tag{9}$$

where C_e signifies the concentration of TCs at equilibrium, measured in mg L^{-1}, while q_e represents the adsorbed amount at equilibrium, expressed in mg g^{-1}. The parameter q_m reflects the maximum adsorption capacity of GO/Co–Fe at monolayer coverage, specified in mg g^{-1}. K_L is the dimensionless Langmuir adsorption constant and K_F is the Freundlich adsorption constant measured in $mg^{1-1/n}$ $L^{-1/n}$ g^{-1}. The parameter 'n' is a constant associated with the adsorption intensity. R is the universal gas constant in joules per Kelvin per mole (J K^{-1} mol^{-1}) and 'T' denotes the temperature in Kelvin (K). These parameters are instrumental in elucidating the interactions between TCs and the GO/Co–Fe adsorbent and the capacity of the adsorbent to adsorb TCs.

Fig. 7(a)–(d) show the Langmuir isotherm models and Fig. 8(a)–(d) depict the Freundlich isotherm models for TC, CTC, OTC, and DTC. The parameters obtained from isotherm

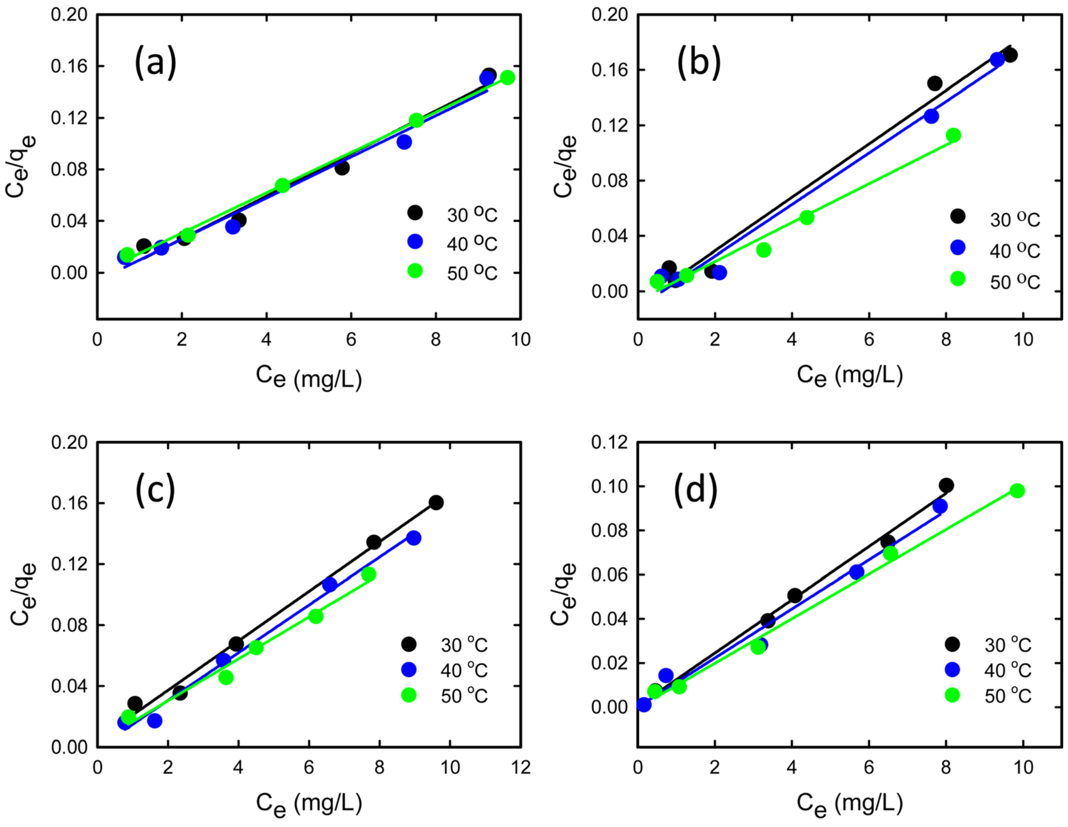

Fig. 7 Linear form of the Langmuir isotherm model for (a) TC, (b) CTC, (c) OTC, and (d) DTC (pH = 7, GO/Co–Fe = 0.15 g L^{-1}, t = 0.5 min, shaking = 250 rpm, T = 30, 40 and 50 °C).

© 2024 The Author(s). Published by the Royal Society of Chemistry

Open Access Article. Published on 03 January 2024. Downloaded on 2/17/2026 1:33:08 PM.
This article is licensed under a Creative Commons Attribution-NonCommercial 3.0 Unported Licence.

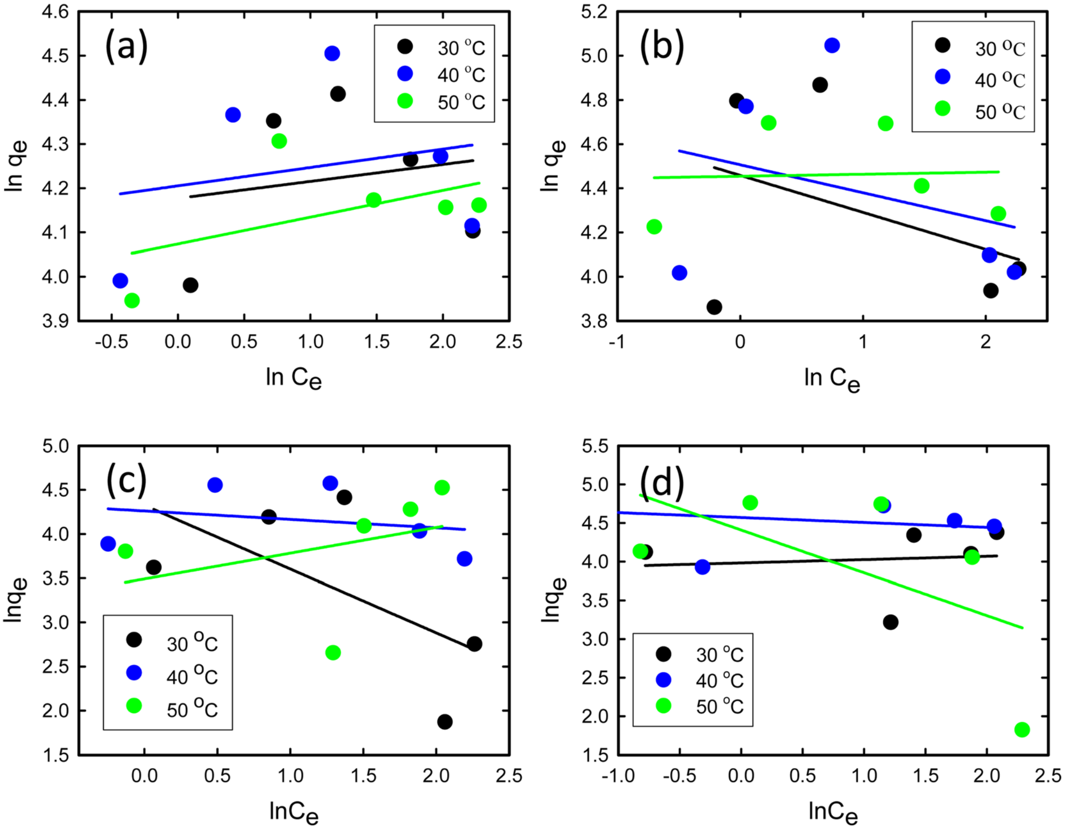

Fig. 8 Linear form of the Freundlich isotherm model for (a) TC, (b) CTC, (c) OTC, and (d) DTC (pH = 7, GO/Co–Fe = 0.15 g L^{-1}, t = 0.5 min, shaking = 250 rpm, T = 30, 40 and 50 °C).

Table 2 Parameters derived from isotherm models

			Temperature (°C)		
Isotherm model	Antibiotic	Parameters	30	40	50
Langmuir	TC	q_m (mg g^{-1})	60.24	62.50	64.10
		K_L (L mg^{-1})	140.8	169.9	1428
		R^2	0.9792	0.9781	0.9980
	CTC	q_m (mg g^{-1})	51.81	53.76	71.43
		K_L (L mg^{-1})	108.7	85.47	153.8
		R^2	0.9832	0.9840	0.9786
	OTC	q_m (mg g^{-1})	61.73	63.69	72.46
		K_L (L mg^{-1})	3.44	19.625	4.92
		R^2	0.9927	0.9910	0.9801
	DTC	q_m (mg g^{-1})	82.64	90.09	99.01
		K_L (L mg^{-1})	30.25	157.33	33.67
		R^2	0.9931	0.9797	0.9935
Freundlich	TC	K_F (mg$^{1-1/n}$ L$^{-1/n}$ g^{-1})	65.17	67.04	58.78
		n	25.97	23.98	16.50
		R^2	0.0324	0.0514	0.2459
	CTC	K_F (mg$^{1-1/n}$ L$^{-1/n}$ g^{-1})	86.37	90.62	86.01
		n	−5.97	−7.89	108.69
		R^2	0.1555	0.0987	0.0021
	OTC	K_F (mg$^{1-1/n}$ L$^{-1/n}$ g^{-1})	75.56	70.88	32.82
		n	−1.39	−10.48	3.43
		R^2	0.3784	0.0600	0.1166
	DTC	K_F (mg$^{1-1/n}$ L$^{-1/n}$ g^{-1})	53.65	96.61	82.10
		n	23.26	−15.67	−1.81
		R^2	0.0108	0.0643	0.3440

© 2024 The Author(s). Published by the Royal Society of Chemistry

Open Access Article. Published on 03 January 2024. Downloaded on 2/17/2026 1:33:08 PM.
This article is licensed under a Creative Commons Attribution-NonCommercial 3.0 Unported Licence.

models are shown in Table 2. Based on the correlation coefficient (R^2) values obtained from fitting the data to various isotherm models, the Langmuir linear model demonstrated the most favourable fit for TCs. The excellent fit of the adsorption data to the Langmuir isotherm indicates that the adsorption of TCs by GO/Co–Fe follows a monolayer adsorption mechanism, which is applicable to heterogeneous surfaces. This implies that a single layer of TC molecules adheres to the adsorbent surface, and further adsorption primarily occurs through lateral interactions between the adsorbate molecules. It is also observed that as the temperature increases, the maximum adsorption capacity (q_m) also increases. This finding suggests that higher temperatures promote a more favourable adsorption process. The rise in maximum adsorption capacity with temperature can be explained by multiple factors. The elevated temperature enhances the molecular mobility of the TC molecules, allowing for greater contact and engagement with the active sites on the GO/Co–Fe adsorbent's surface. Moreover, the increased kinetic energy of the molecules facilitates their diffusion into the adsorbent, leading to a higher adsorption capacity.[51] The maximum adsorption capacity for GO/Co–Fe was calculated to be 64.10 mg g^{-1} (TC), 71.43 mg g^{-1} (CTC), 72.46 mg g^{-1} (OTC), and 99.01 mg g^{-1} (DTC).

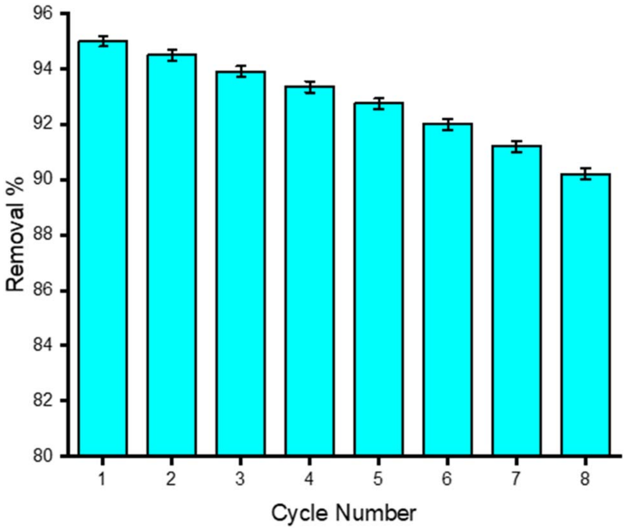

Fig. 9 Stability and reusability tests for the adsorbent, GO/Co–Fe.

3.2.7 Stability and reusability study. Following the adsorption of TCs, the GO/Co–Fe adsorbent was successfully separated with the application of an external magnetic field. Subsequently, the adsorbent was regenerated through methanol treatment. Remarkably, the GO/Co–Fe adsorbent exhibited excellent reusability and recyclability, as demonstrated in Fig. 9. The findings showed that the adsorbent could be recycled for up to 8 rounds, with a minor reduction in removal efficiency, dropping from 95% to 90%. It is noteworthy to highlight some recent studies that achieved higher recycling rounds using a higher dosage of adsorbent (>> 0.15 g L^{-1}) with an equilibrium time of several hours.[52–55] In contrast, our current investigation utilized a notably lower adsorbent dosage (0.15 g L^{-1}) and achieved a faster equilibrium time of only 30 s. This demonstrates the efficiency and practicality of the GO/Co–Fe adsorbent, which not only competes favourably with recent studies but also does so with a substantially reduced adsorbent quantity and a significantly shorter equilibrium time. The reusability capability highlights the potential of the GO/Co–Fe adsorbent as an efficient and environment friendly solution for eliminating TCs from water sources, offering economic and environmental benefits through its repeated utilisation.

3.2.8 Comparison of GO/Co–Fe adsorbents with other adsorbents. This comparative study, outlined in Table 3, evaluates the adsorption capacities of various adsorbents including illite, amino-Fe(III)-functionalized SBA15, hazelnut shell-derived activated carbons, Fe-doped zeolite, nitrilotriacetic acid-functionalized magnetic graphene oxide, and chitosan-olive pomace adsorbing films. Notably, the GO/Co–Fe magnetic nanocomposite, highlighted in this investigation, demonstrates strong performance with adsorption capacities of 64.10 mg g^{-1} for TC, 71.43 mg g^{-1} for CTC, 72.46 mg g^{-1} for OTC, and 99.01 mg g^{-1} for DTC. The nanocomposite exhibits a rapid equilibrium within 30 s and optimal adsorption at pH 7, positioning it as a standout adsorbent for swift and effective contaminant removal. These findings, as presented in Table 3, underscore the potential of the GO/Co–Fe magnetic nanocomposite in comparison to other adsorbents, emphasizing its promising applications in diverse environmental remediation scenarios.

Table 3 Adsorption capacities and time required to reach equilibrium of various adsorbents used in removal of tetracyclines

Adsorbent	Adsorption Capacity, q_m (mg g^{-1})	Equilibrium time	Temperature (°C)	pH	Ref.
Illite	32	8 h	25	5–6	56
Amino-Fe(III) functionalized SBA15	65.98	24 h	25	4.5–5.6	57
Hazelnut shell derived activated carbons	321.5	20 min	20	4–8	58
Fe-doped zeolite	204	24 h	25	6	59
Nitrilotriacetic acid-functionalized magnetic graphene oxide	212	24 h	25	4	60
Chitosan-olive pomace adsorbing films	16	1 h	27	8	61
Waste-material derived GO/Co–Fe magnetic nanocomposite	**TC = 64.10** **CTC = 71.43** **OTC = 72.46** **DTC = 99.01**	**30 seconds**	**25**	**7**	**This study**

Open Access Article. Published on 03 January 2024. Downloaded on 2/17/2026 1:33:08 PM.
This article is licensed under a Creative Commons Attribution-NonCommercial 3.0 Unported Licence.

4 Conclusion

In conclusion, a magnetically separable GO/Co–Fe composite has been synthesized successfully. Various analytical techniques suggest the well-dispersed nanoparticles (19.2 nm) and a superparamagnetic nature with saturation magnetization (27.82 emu g^{-1}) of the prepared composite. The adsorption studies of GO/Co–Fe for the removal of TCs revealed that GO/Co–Fe achieved maximum removal efficiencies of 93.94% for TC, 95.51% for CTC, 93.21% for OTC, and 91.12% for DTC just within 30 s at neutral pH and with a low adsorbent dose of 0.15 g L^{-1}, while the initial concentration of TCs were 0.2 mg L^{-1}. The adsorption kinetics followed the pseudo-second-order kinetic model, suggesting the interaction of TCs with GO/Co–Fe *via* hydrogen bonding as well as electrostatic interaction, and the adsorption was mainly governed by the chemisorption process. The isotherm data for the adsorption process were modelled using the Langmuir isotherm, suggesting that the adsorption occurs as a monolayer on the adsorbent surface. The maximum adsorption capacity of GO/Co–Fe was found to be 64.10 (TC), 71.43 (CTC), 72.46 (OTC), and 99.01 mg g^{-1} (DTC). Furthermore, the GO/Co–Fe adsorbent demonstrated excellent reusability, retaining its efficiency even after eight cycles of use, with only a minor decrease in removal efficiency. The successful removal of antibiotics using waste material-derived GO-based magnetic composites opens up possibilities for their use in water treatment, aiding in the purification of antibiotic-contaminated water sources.

Author contributions

Md Sohag Hossain: experimental execution, data analysis, writing original draft. Md Humayun Kabir: conceptualization, methodology, writing, editing, project administration, supervision of the work. Md Aftab Ali Shaikh: review, editing and managed the funding with required facilities. Md Anamul Haque: data analysis, review & editing. Sabina Yasmin: conceptualization, methodology, writing, review & editing. and supervision of the work.

Conflicts of interest

The authors declare no competing interest.

Acknowledgements

The authors are grateful to Bangladesh Council of Scientific and Industrial Research (BCSIR) authority for financial support (R&D ref. no. 39.02.0000.011.14.169.2023/877, date 17.09. 2023) and facilities. The assistance from CARF, IERD, and BAEC to acquire XRD, Zeta potential, SEM-EDX and TEM is appreciated.

References

1 T. T. H. Van, Z. Yidana, P. M. Smooker and P. J. Coloe, *J. Global Antimicrob. Resist.*, 2020, **20**, 170–177.
2 L. F. Angeles, S. Islam, J. Aldstadt, K. N. Saqeeb, M. Alam, M. A. Khan, F.-T. Johura, S. I. Ahmed and D. S. Aga, *Sci. Total Environ.*, 2020, **712**, 136285.
3 M. Bilal, S. Mehmood, T. Rasheed and H. M. N. Iqbal, *Curr. Opin. Environ. Sci. Health*, 2020, **13**, 68–74.
4 J. E. Sosa-Hernández, L. I. Rodas-Zuluaga, I. Y. López-Pacheco, E. M. Melchor-Martínez, Z. Aghalari, D. S. Limón, H. M. N. Iqbal and R. Parra-Saldívar, *Case Stud. Chem. Environ. Eng.*, 2021, **4**, 100127.
5 J. Li, Y. Wang, Z. Fan, P. Tang, M. Wu, H. Xiao and Z. Zeng, *Int. J. Environ. Res. Public Health*, 2023, **20**, 3623.
6 N. U. Barbhuyan, D. Tayeng, N. Gogoi, L. Patowary, D. Chetia and M. S. Barthakur, *Sci. Phytochem.*, 2023, **2**, 8–16.
7 C. D. Iwu, L. Korsten and A. I. Okoh, *MicrobiologyOpen*, 2020, **9**, e1035.
8 Y. Amangelsin, Y. Semenova, M. Dadar, M. Aljofan and G. Bjørklund, *Antibiotics*, 2023, **12**, 440.
9 G. Zhang, X. Sui, Y. Xu, Y. Jiao, J.-S. Chang and D.-J. Lee, *Bioresour. Technol.*, 2022, **346**, 126677.
10 S. Shao and X. Wu, *Crit. Rev. Biotechnol.*, 2020, **40**, 1010–1018.
11 F. Baghal Asghari, M. H. Dehghani, R. Dehghanzadeh, D. Farajzadeh, D. Shanehbandi, A. H. Mahvi, K. Yaghmaeian and A. Rajabi, *Sci. Rep.*, 2021, **11**, 24519.
12 J. Zambrano, P. A. García-Encina, J. J. Jiménez, R. López-Serna and R. Irusta-Mata, *J. Water Process Eng.*, 2022, **48**, 102841.
13 J. Wang, S. Lei and L. Liang, *Appl. Surf. Sci.*, 2020, **530**, 147187.
14 K. D. Burch, B. Han, J. Pichtel and T. Zubkov, *Environ. Sci. Pollut. Res.*, 2019, **26**, 6301–6310.
15 X. Guo, P. Wang, Y. Li, H. Zhong, P. Li, C. Zhang and T. Zhao, *Bioresour. Technol.*, 2019, **291**, 121916.
16 J. Wang and R. Zhuan, *Sci. Total Environ.*, 2020, **701**, 135023.
17 R. K. Langbehn, C. Michels and H. M. Soares, *Environ. Pollut.*, 2021, **275**, 116603.
18 J. Gu, Z. Liu, A. Jia, Y. Wang, N. Li, Z. Liu, Y. Li and H. Zhang, *Sep. Purif. Technol.*, 2023, **312**, 123408.
19 S. Barakan and V. Aghazadeh, *Environ. Sci. Pollut. Res.*, 2021, **28**, 2572–2599.
20 A. Maged, J. Iqbal, S. Kharbish, I. S. Ismael and A. Bhatnagar, *J. Hazard. Mater.*, 2020, **384**, 121320.
21 A. Yazidi, M. Atrous, F. Edi Soetaredjo, L. Sellaoui, S. Ismadji, A. Erto, A. Bonilla-Petriciolet, G. Luiz Dotto and A. Ben Lamine, *Chem. Eng. J.*, 2020, **379**, 122320.
22 C. Xia, H. Huang, D. Liang, Y. Xie, F. Kong, Q. Yang, J. Fu, Z. Dou, Q. Zhang and Z. Meng, *Chem. Eng. J.*, 2022, **443**, 136398.
23 D. Xie, H. Zhang, M. Jiang, H. Huang, H. Zhang, Y. Liao and S. Zhao, *Chin. J. Chem. Eng.*, 2020, **28**, 2689–2698.
24 Y. Ai, Y. Liu, Y. Huo, C. Zhao, L. Sun, B. Han, X. Cao and X. Wang, *Environ. Sci.: Nano*, 2019, **6**, 3336–3348.
25 M.-L. Cui, Z.-X. Lin, Q.-F. Xie, X.-Y. Zhang, B.-Q. Wang, M.-L. Huang and D.-P. Yang, *Food Chem.*, 2023, **412**, 135554.
26 Md. G. Azam, M. H. Kabir, Md. A. A. Shaikh, S. Ahmed, M. Mahmud and S. Yasmin, *J. Water Process Eng.*, 2022, **46**, 102597.

© 2024 The Author(s). Published by the Royal Society of Chemistry

Open Access Article. Published on 03 January 2024. Downloaded on 2/17/2026 1:33:08 PM.
This article is licensed under a Creative Commons Attribution-NonCommercial 3.0 Unported Licence.

27 S. Yasmin, M. S. Ahmed and S. Jeon, *J. Nanosci. Nanotechnol.*, 2017, **17**, 3959–3966.

28 B. P. Upoma, S. Yasmin, Md. A. Ali Shaikh, T. Jahan, Md. A. Haque, M. Moniruzzaman and M. H. Kabir, *ACS Omega*, 2022, **7**, 29655–29665.

29 F. Monehzadeh and Z. Rafiee, *Appl. Organomet. Chem.*, 2020, **34**, e5631.

30 Y. Peng, Z. Chen, R. Zhang, W. Zhou, P. Gao, J. Wu, H. Liu, J. Liu, A. Hu and X. Chen, *Nano-Micro Lett.*, 2021, **13**, 192.

31 W. Gao, M. Majumder, L. B. Alemany, T. N. Narayanan, M. A. Ibarra, B. K. Pradhan and P. M. Ajayan, *ACS Appl. Mater. Interfaces*, 2011, **3**, 1821–1826.

32 D. Wang, L. Liu, X. Jiang, J. Yu and X. Chen, *Colloids Surf., A*, 2015, **466**, 166–173.

33 N. Rattanachueskul, A. Saning, S. Kaowphong, N. Chumha and L. Chuenchom, *Bioresour. Technol.*, 2017, **226**, 164–172.

34 M. A. Salam, R. M. El-Shishtawy and A. Y. Obaid, *J. Ind. Eng. Chem.*, 2014, **20**, 3559–3567.

35 S. Yasmin, S. Cho and S. Jeon, *Appl. Surf. Sci.*, 2018, **434**, 905–912.

36 S. Yasmin, Y. Joo and S. Jeon, *Appl. Surf. Sci.*, 2017, **406**, 226–234.

37 S. Yasmin, M. Shamsuddin Ahmed and S. Jeon, *Int. J. Hydrogen Energy*, 2017, **42**, 1075–1084.

38 Y. Zhang, Z. Jiao, Y. Hu, S. Lv, H. Fan, Y. Zeng, J. Hu and M. Wang, *Environ. Sci. Pollut. Res.*, 2017, **24**, 2987–2995.

39 H.-L. Guo, X.-F. Wang, Q.-Y. Qian, F.-B. Wang and X.-H. Xia, *ACS Nano*, 2009, **3**, 2653–2659.

40 G. Xian, S. Kong, Q. Li, G. Zhang, N. Zhou, H. Du and L. Niu, *Front. Chem.*, 2020, **8**, 177.

41 S. Yasmin, M. H. Kabir, N. Roy and S. Jeon, *ECS adv.*, 2023, **2**, 024504.

42 N. Roy, S. Yasmin and S. Jeon, *Microchem. J.*, 2020, **153**, 104501.

43 N. Roy, S. Yasmin, A. Ejaz, H. Soon Han and S. Jeon, *Appl. Surf. Sci.*, 2020, **533**, 147500.

44 S. Yasmin, N. Roy, M. H. Kabir and S. Jeon, *Appl. Surf. Sci. Adv.*, 2022, **9**, 100235.

45 A. K. Mohiuddin, S. Yasmin and S. Jeon, *Sens. Actuators, A*, 2023, **355**, 114314.

46 N. Roy, S. Yasmin, A. K. Mohiuddin and S. Jeon, *Appl. Surf. Sci. Adv.*, 2023, **18**, 100517.

47 S. Yasmin, M. H. Kabir, M. A. A. Shaikh and S. Jeon, *ECS J. Solid State Sci. Technol.*, 2023, **12**, 111004.

48 S. Yasmin, M. S. Ahmed, D. Park and S. Jeon, *J. Electrochem. Soc.*, 2016, **163**, B491.

49 S. Yasmin, M. S. Ahmed and S. Jeon, *J. Electrochem. Soc.*, 2015, **162**, B363.

50 D. Qiao, Z. Li, J. Duan and X. He, *Chem. Eng. J.*, 2020, **400**, 125952.

51 J. Wang, H. Huang, M. Wang, L. Yao, W. Qiao, D. Long and L. Ling, *Ind. Eng. Chem. Res.*, 2015, **54**, 5319–5327.

52 Y. Jaqueline Fachina, E. Freitas Diogo Januário, M. Barbosa de Andrade, L. Fernando Cusioli, R. Bergamasco and A. Marquetotti Salcedo Vieira, *Environ. Nanotechnol., Monit. Manage.*, 2023, **20**, 100890.

53 J. Tang, L. Zong, B. Mu, Y. Kang and A. Wang, *Korean J. Chem. Eng.*, 2018, **35**, 1650–1661.

54 Y. Zhang, Z. Jiao, Y. Hu, S. Lv, H. Fan, Y. Zeng, J. Hu and M. Wang, *Environ. Sci. Pollut. Res.*, 2017, **24**, 2987–2995.

55 A. Pardo, H. Garcia, P. Ramirez, M. A. Carrillo-Alvarado, K. S. Krishna, N. Dominguez, M. T. Islam, H. Wang and J. C. Noveron, *Environ. Technol. Innovation*, 2018, **11**, 321–327.

56 P.-H. Chang, Z. Li, J.-S. Jean, W.-T. Jiang, C.-J. Wang and K.-H. Lin, *Appl. Clay Sci.*, 2012, **67–68**, 158–163.

57 Z. Zhang, H. Lan, H. Liu and J. Qu, *Colloids Surf., A*, 2015, **471**, 133–138.

58 H.-T. Fan, L.-Q. Shi, H. Shen, X. Chen and K.-P. Xie, *RSC Adv.*, 2016, **6**, 109983–109991.

59 M. H. Jannat Abadi, S. M. M. Nouri, R. Zhiani, H. D. Heydarzadeh and A. Motavalizadehkakhky, *Int. J. Ind. Chem.*, 2019, **10**, 291–300.

60 M. Li, Y. Liu, G. Zeng, S. Liu, X. Hu, D. Shu, L. Jiang, X. Tan, X. Cai and Z. Yan, *J. Colloid Interface Sci.*, 2017, **485**, 269–279.

61 V. Rizzi, D. Lacalamita, J. Gubitosa, P. Fini, A. Petrella, R. Romita, A. Agostiano, J. A. Gabaldón, M. I. Fortea Gorbe, T. Gómez-Morte and P. Cosma, *Sci. Total Environ.*, 2019, **693**, 133620.

© 2024 The Author(s). Published by the Royal Society of Chemistry